

PAPER

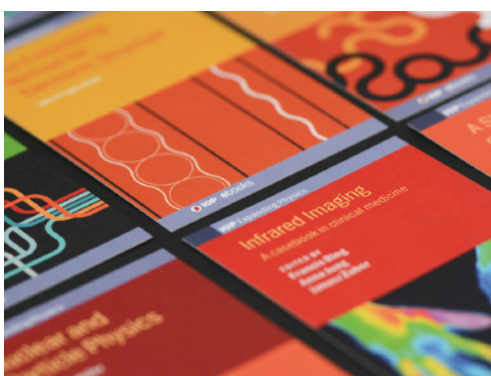
Analyzing effects of temperature gradient and scan rate on metal additive manufacturing microstructure by using phase field-finite element method

To cite this article: Liu Cao *et al* 2022 *Modelling Simul. Mater. Sci. Eng.* **30** 034003

View the [article online](#) for updates and enhancements.

You may also like

- [Thermal characterization of a single microdischarge in atmospheric pressure air dielectric barrier discharges](#)
K-M Lin, S-Y Chuang, W-Y Guo *et al.*
- [Isomorphic contact resonance force microscopy and piezoresponse force microscopy of an AlN thin film: demonstration of a new contact resonance technique](#)
Lawrence H Robins, Matt D Brubaker, Ryan C Tung *et al.*
- [Crystallographic polarity measurements in two-terminal GaN nanowire devices by lateral piezoresponse force microscopy](#)
Matt D Brubaker, Alexana Roshko, Samuel Berweger *et al.*



IOP | ebooks™

Bringing together innovative digital publishing with leading authors from the global scientific community.

Start exploring the collection—download the first chapter of every title for free.

Analyzing effects of temperature gradient and scan rate on metal additive manufacturing microstructure by using phase field-finite element method

Liu Cao^{1,*} , Luo Zhang², Rui-Fan Meng¹  and Qin-Dan Zhang¹

¹ Institute for Systems Rheology, School of Mechanical and Electrical Engineering, Guangzhou University, Guangzhou Higher Education Mega Center, Guangzhou, Guangdong 510006, People's Republic of China

² School of Mechanical Engineering, University of Science and Technology Beijing, Beijing 100089, People's Republic of China

E-mail: caoliu@gzhu.edu.cn

Received 15 September 2021, revised 21 December 2021

Accepted for publication 26 January 2022

Published 16 February 2022



CrossMark

Abstract

Predicting the evolutionary behavior of microstructures with the help of numerical simulation techniques has become an essential tool for studying the solidification process of metal additive manufacturing. As a mesoscopic model based on the diffusion interface theory, phase field method (PFM) can be used to predict the evolution of solidification microstructure. The open-source PFM framework PRISMS-PF can not only efficiently solve systems of equations with billions of degrees of freedom, but also provide a simple adaptive mesh control module. In this paper, based on the open-source PFM framework PRISMS-PF, a phase field-finite element method (PFM-FEM) simulation flow for the solidification process of A356 aluminum alloy additive manufacturing in the two-dimensional case was established. The effects of temperature gradient, scan rate and initial solid-phase morphology on solute concentration, dendrite spacing and dendrite morphology were analyzed and compared with experimental results for verification. Analyzing the results for different temperature gradients and scan rates cases, it was found that the increase of temperature gradient or scan rate made the primary dendrite arm space decrease; as the ratio of temperature gradient to scan rate decreased, the solidification morphology gradually changed from flat crystal to cellular crystal, columnar crystal, and even

*Author to whom any correspondence should be addressed.

dendritic structure. Analyzing the results for different initial solid-phase morphology cases, it was found that the influence of initial solid-phase morphology on dendrite growth increased as the ratio of temperature gradient to scan rate decreased. The above influence rules were mainly related to the composition overcooling zone under different conditions. This paper is expected to provide a theoretical support for the effective regulation of solidification microstructure in metal additive manufacturing.

Keywords: phase field-finite element method, metal additive manufacturing, temperature gradient, scan rate, dendrite spacing, dendrite morphology

(Some figures may appear in colour only in the online journal)

Nomenclature

τ_ϕ	Coefficient of the left-end term of equation (1)
t	Dimensionless time
τ_U	Coefficient of the left-end term of equation (2)
\tilde{D}	Dimensionless solute diffusion coefficient in the liquid-phase
\tilde{J}_{at}^U	For characterizing the effect of phase transition on solute distribution
k	Solute redistribution coefficient
$a(\hat{n})$	Interface energy anisotropy function
x, y	Dimensionless horizontal and vertical coordinates
λ	Dimensionless coupling parameter
U_{off}	Determining the initial overcooling degree of the liquid–solid interface, $U_{off} = 0$ indicates that the initial temperature of the liquid–solid interface is the solidus temperature, and $U_{off} = 1$ indicates that the initial temperature of the liquid–solid interface is the liquidus temperature
y_0	Dimensionless longitudinal height of the initial liquid–solid interface
\tilde{V}_p	Dimensionless scan rate
\tilde{l}_T	Dimensionless thermal action length, characterizing the effect of temperature gradient on solidification behavior
\hat{n}	Unit normal vector at the liquid–solid interface (from the solid-phase to the liquid-phase)
ε_m	Anisotropic strength
m	Crystal system parameter, $m = 4$ denotes the cubic crystal system, and $m = 6$ denotes the hexagonal crystal system
θ	Grain growth angle
θ_0	Deflection angle of grain growth
\hat{x}, \hat{y}	Unit normal vectors in the horizontal and vertical directions, respectively
c	Solute concentration, %
c_0	Initial liquid-phase solute concentration, %
U_0	Initial dimensionless supersaturation concentration, and $U_0 = -1$ denotes the initial liquid-phase solute concentration of c_0 and the initial solid-phase solute concentration of kc_0
a_1, a_2	Constants with values of 0.8839 and 0.6267, respectively
d_0	Capillary action length, m

W	Artificially specified liquid–solid interface thickness, which is selected as the characteristic length, and its value is usually in the range of $10d_0$ to $100d_0$, m
V_p	Scan rate (pulling rate), m s^{-1}
D	Solute diffusion coefficient in the liquid-phase, $\text{m}^2 \text{s}^{-1}$
m_l	Rate of change of liquidus temperature with solute concentration, $\text{K}/\%$
G	Temperature gradient, K m^{-1}
τ_0	Characteristic time, s
γ_0	Surface tension coefficient, N m^{-1}
T_m	Melting point, K
c_p	Specific heat capacity, $\text{J (kg}^{-1} \text{K}^{-1})$
ρ	Density, kg m^{-3}
L	Latent heat of solidification, J kg^{-1}
Superscripts $n, n + 1$	Denote the values of the physical quantities at the current moment and after a certain time step, respectively
r_ϕ	Right-end term coefficient of the FE weak form of ϕ
r_U, \hat{r}_{Ux}	Right-end term coefficients of the FE weak form of U
$r_\xi, \hat{r}_{\xi x}$	Right-end term coefficients of the FE weak form of ξ
Δt	Dimensionless time step

1. Introduction

Metal additive manufacturing (3D printing) is considered to be one of the most valuable technologies in the additive manufacturing system, which has the advantages of lightweight, integration and mold-free manufacturing that are difficult to achieve with traditional thermal-mechanical processing methods. At the same time, it can greatly meet the needs of high performance, rapidity, flexibility, customization and eco-friendly put forward by future intelligent manufacturing equipment [1, 2]. As the requirements for mechanical properties of metal additive manufacturing parts increase, researchers are becoming more aware of the importance of the ‘process-microstructure-property’ interrelationship [3, 4]. However, the molten pool in the metal additive manufacturing process is often a tiny region of high temperature and high transients, making it difficult to directly observe the microstructure evolution behavior during solidification by experimental means [5, 6]. Therefore, predicting the evolutionary behavior of microstructures with the help of numerical simulation techniques has become a necessary tool to study the solidification process of metal additive manufacturing [7–9].

For microstructure prediction of solidification processes in metal additive manufacturing, the mainstream numerical simulation methods currently include cellular automaton method [10, 11] (CAM), Monte Carlo method (MCM) [12, 13], and phase field method [14, 15] (PFM). Among them, CAM is based on macroscopic (millimeter scale) solidification thermodynamics and grain nucleation and growth kinetics, and can be used to analyze the effects of overcooling and solute concentration on the solidification microstructure [16]. Lian *et al* [17] used a combination of CAM and finite volume method to predict the three-dimensional multilayer grain morphology and reveal the typical epitaxial crystallization behavior and the ‘sandwich’ and ‘jagged’ grain arrangement in metal additive manufacturing process. CAM can calculate the solidification process in a large size range, but its ability to describe the solidification structure morphology is weak, and it can only predict the grain growth process approximately. With CAM it is difficult to deal with the effect of interfacial curvature on the grain growth rate, and it is more sensitive to the shape and size of the cell [18]. MCM is based on the principle of minimum interface energy, with probability statistics as the main theoretical basis and

random sampling as the main means. MCM has the advantage of describing the grain growth process by a simple probabilistic statistical model, but it lacks a reliable basis for solidification kinetics [19]. PFM is a mesoscopic (micrometer scale) model based on the diffusion interface theory, which avoids tracing the solid–liquid interface with complex morphology and can effectively couple solute, temperature, flow and other external fields, basically reproducing the evolution of solidification microstructure [20]. Zhang *et al* [21] used PFM to predict the solidification process of Ti-6Al-4V alloy for additive manufacturing, and analyzed the effects of temperature gradient and scan rate on the dendrite morphology and growth rate, and found that high temperature gradient and scan rate helped to obtain small dendrite spacing and high dendrite growth rate. The controlling equations of nucleation, growth and coarsening in PFM have the same mathematical form, and with PFM it can obtain sufficiently fine dendrite morphology, but the computational efficiency needs to be improved [22].

To address the low efficiency of PFM calculation, the mainstream improvement methods currently include adaptive mesh [23] and parallel calculation [24]. Guo *et al* [25] proposed a dynamic re-meshing strategy based on the maximum interface advance rate for the prediction of dendrite growth in the three-dimensional case, and the results showed that the computational efficiency was improved by two orders of magnitude. Ding *et al* [26] proposed a parallel acceleration algorithm based on a dynamic computational domain partitioning strategy for the PF simulation of solidification process, which improved the computational efficiency to a certain extent. However, the vast majority of currently available PFM codes are close-source, resulting in a high barrier to conducting PFM research on metal additive manufacturing processes for a long time. In recent years, some PFM open-source community frameworks have emerged, such as MOOSE [27], OpenPhase [28], FiPy [29], MMSP [30], and PRISMS-PF [31]. Among them, University of Michigan launched the open-source PFM framework PRISMS-PF [32] in 2018, and after nearly four years of iterative development, PRISMS-PF provides a customizable system of partial differential equations for solving PF models to predict various types of microstructural evolution processes such as grain nucleation, growth, coarsening, and solid-state phase transitions. Meanwhile, PRISMS-PF not only provides a simple adaptive mesh control module, but also takes advantage of the matrix-free feature of the Deal.II finite element library [33], which eliminates the need to store and access the global sparse matrix vector product and can efficiently solve systems of equations with billions of degrees of freedom. The open-source framework PRISMS-PF provides the so-called phase field-finite element method (PFM-FEM) simulation flow, which can be a fundamental tool for solidification microstructure simulation in metal additive manufacturing.

In this paper, a simulation study of the binary alloy additive manufacturing process in the two-dimensional case was carried out based on the open-source PFM framework PRISMS-PF. The effects of temperature gradient, scan rate and initial solid-phase morphology on solute concentration, dendrite spacing and dendrite morphology were calculated and analyzed for the study of the additive manufacturing process of A356 aluminum alloy, and compared with the experimental results for verification. This paper is expected to provide a theoretical support for the effective regulation of solidification microstructure in metal additive manufacturing.

2. PFM-FEM model for binary alloy additive manufacturing process

2.1. PFM for binary alloy additive manufacturing process

Considering the high temperature gradient and epitaxial crystallization characteristics of the metal additive manufacturing solidification process, it is a common practice to equate the metal

additive manufacturing solidification process to a directional solidification process, and then to equate the metal additive manufacturing solidification conditions by adjusting the temperature gradient and the scan rate (pulling rate) [21]. The problem scenario addressed here is the gradual growth of an initial solid-phase region under directional solidification conditions in the two-dimensional case. Therefore, there are three required PF variables: first, the liquid–solid phase variable ϕ ($\phi = 1$ for the solid-phase, $\phi = -1$ for the liquid-phase, and $-1 < \phi < 1$ for the liquid–solid interface), second, the dimensionless supersaturation concentration U , and third, the intermediate variable ξ . It should be noted that the intermediate variable ξ is proposed to make the derivation and calculation process of the PFM more clear and straightforward.

The controlling equations for the PF variables ϕ , U and ξ are [34]:

$$\tau_\phi \frac{\partial \phi}{\partial t} = \xi(\phi, U) \quad (1)$$

$$\tau_U \frac{\partial U}{\partial t} = \nabla \cdot [\tilde{D}(1 - \phi) \nabla U + \vec{j}_{at}^U] + [1 + (1 - k)U] \frac{\partial \phi}{\partial t} \quad (2)$$

$$\begin{aligned} \xi(\phi, U) = & \nabla \cdot [a^2(\hat{n}) \nabla \phi] + \frac{\partial}{\partial x} \left[|\nabla \phi|^2 a(\hat{n}) \frac{\partial a(\hat{n})}{\partial (\partial \phi / \partial x)} \right] + \frac{\partial}{\partial y} \left[|\nabla \phi|^2 a(\hat{n}) \frac{\partial a(\hat{n})}{\partial (\partial \phi / \partial y)} \right] \\ & + \phi - \phi^3 - \lambda(1 - \phi^2)^2 \left[U + U_{\text{off}} + \frac{y - y_0 - \tilde{V}_p t}{\tilde{l}_T} \right] \end{aligned} \quad (3)$$

in which:

$$\tau_\phi = [1 + (1 - k)U] a^2(\hat{n}) \quad (4)$$

$$\tau_U = 1 + k - (1 - k)\phi \quad (5)$$

$$\vec{j}_{at}^U = -\frac{1}{\sqrt{2}} [1 + (1 - k)U] \frac{\partial \phi}{\partial t} \hat{n} \quad (6)$$

$$\hat{n} = -\frac{\nabla \phi}{|\nabla \phi|} \quad (7)$$

$$a(\hat{n}) = 1 + \varepsilon_m \cos[m(\theta - \theta_0)] \quad (8)$$

$$\tan(\theta) = \frac{\partial \phi / \partial y}{\partial \phi / \partial x}. \quad (9)$$

From equations (8) and (9), it follows that:

$$\frac{\partial a(\hat{n})}{\partial (\partial\phi/\partial x)} = \frac{\varepsilon_m m \sin[m(\theta - \theta_0)] \frac{\partial\phi}{\partial y}}{|\nabla\phi|^2} \quad (10)$$

$$\frac{\partial a(\hat{n})}{\partial (\partial\phi/\partial y)} = -\frac{\varepsilon_m m \sin[m(\theta - \theta_0)] \frac{\partial\phi}{\partial x}}{|\nabla\phi|^2}. \quad (11)$$

Substituting equations (10) and (11) into (3) yields:

$$\begin{aligned} \xi(\phi, U) = \nabla \cdot & \left[\begin{aligned} & \left\{ a^2(\hat{n}) \frac{\partial\phi}{\partial x} + a(\hat{n}) \varepsilon_m m \sin[m(\theta - \theta_0)] \frac{\partial\phi}{\partial y} \right\} \hat{x} \\ & + \left\{ a^2(\hat{n}) \frac{\partial\phi}{\partial y} - a(\hat{n}) \varepsilon_m m \sin[m(\theta - \theta_0)] \frac{\partial\phi}{\partial x} \right\} \hat{y} \end{aligned} \right] \\ & + \phi - \phi^3 - \lambda(1 - \phi^2)^2 \left[U + U_{\text{off}} + \frac{y - y_0 - \tilde{V}_p t}{\tilde{l}_T} \right] \end{aligned} \quad (12)$$

Substituting equation (1) into (2) yields:

$$\tau_U \frac{\partial U}{\partial t} = \nabla \cdot \left[\tilde{D}(1 - \phi) \nabla U + \vec{j}_{at}^U \right] + [1 + (1 - k)U] \frac{\xi(\phi, U)}{\tau_\phi}. \quad (13)$$

The above equations are dimensionless for solute concentration, time and length, and the correspondences between the dimensionless physical quantities and the actual physical quantities are:

$$c = \frac{c_0 [1 + k - (1 - k)\phi] [1 + (1 - k)U]}{2(1 + U_0 - U_0 k)} \quad (14)$$

$$\tilde{D} = a_1 a_2 \frac{W}{d_0} \quad (15)$$

$$\lambda = a_1 \frac{W}{d_0} \quad (16)$$

$$\tilde{V}_p = a_1 a_2 \frac{V_p W^2}{D d_0} \quad (17)$$

$$\tilde{l}_T = \frac{|m_1| c_0 (1 - k)}{k G W} \quad (18)$$

$$\tau_0 = a_1 a_2 \frac{W^3}{D d_0} \quad (19)$$

$$d_0 = \frac{\gamma_0 T_m c_p}{\rho L^2}. \quad (20)$$

It should be noted that the characteristic time τ_0 and characteristic length W are both alloy dependent, and the true time and true length can be obtained by multiplying the dimensionless time and dimensionless length by τ_0 and W , respectively. Taking the A356 aluminum

alloy used herein as an example, its characteristic length is 1.77×10^{-7} m and characteristic time is 1.19×10^{-4} s. The temperature gradient G herein refers to the temperature gradient near the solidification interface on the micron scale. For various metal additive manufacturing scenarios, numerical simulation methods can be used to obtain the temperature distribution of the entire solidification process and thus the temperature gradient at each stage. Since this paper targets microstructure prediction, the temperature gradient is given directly.

2.2. FEM for solving the PFM

Based on the PFM-FEM simulation flow provided by PRISMS-PF [31], equations (1), (12) and (13) are first subjected to forward Eulerian explicit time stepping, which in turn leads to the FE weak forms of the PF variables ϕ , U , and ξ as:

$$\int_{\Omega} w \phi^{n+1} dV = \int_{\Omega} w r_{\phi} dV \quad (21)$$

$$\int_{\Omega} w U^{n+1} dV = \int_{\Omega} (w r_U + \nabla w \cdot \hat{r}_{Ux}) dV \quad (22)$$

$$\int_{\Omega} w \xi^{n+1} dV = \int_{\Omega} (w r_{\xi} + \nabla w \cdot \hat{r}_{\xi x}) dV \quad (23)$$

in which:

$$r_{\phi} = \phi^n + \frac{\xi^n}{\tau_{\phi}} \Delta t \quad (24)$$

$$r_U = U^n - \Delta t \nabla \frac{1}{\tau_U} \cdot [\tilde{D}(1 - \phi^n) \nabla U^n + \tilde{J}_{at}^U] + \Delta t \frac{[1 + (1 - k) U^n] \xi^n}{\tau_U \tau_{\phi}} \quad (25)$$

$$\hat{r}_{Ux} = -\frac{\Delta t}{\tau_U} [\tilde{D}(1 - \phi^n) \nabla U^n + \tilde{J}_{at}^U] \quad (26)$$

$$r_{\xi} = \phi^n - (\phi^n)^3 - \lambda(1 - (\phi^n)^2)^2 \left[U^n + U_{off} + \frac{y - y_0 - \tilde{V}_p t}{\tilde{l}_T} \right] \quad (27)$$

$$\begin{aligned} \hat{r}_{\xi x} = & - \left\{ a^2(\hat{n}) \frac{\partial \phi}{\partial x} + a(\hat{n}) \varepsilon_m m \sin [m(\theta^n - \theta_0)] \frac{\partial \phi}{\partial y} \right\} \hat{x} \\ & - \left\{ a^2(\hat{n}) \frac{\partial \phi}{\partial y} - a(\hat{n}) \varepsilon_m m \sin [m(\theta^n - \theta_0)] \frac{\partial \phi}{\partial x} \right\} \hat{y} \end{aligned} \quad (28)$$

From equation (5), it follows that:

$$\nabla \frac{1}{\tau_U} = \frac{1 - k}{(\tau_U)^2} \nabla \phi. \quad (29)$$

Substituting equation (29) into (25) yields:

$$r_U = U^n - \Delta t \frac{1 - k}{(\tau_U)^2} \nabla \phi \cdot [\tilde{D}(1 - \phi^n) \nabla U^n + \tilde{J}_{at}^U] + \Delta t \frac{[1 + (1 - k) U^n] \xi^n}{\tau_U \tau_{\phi}}. \quad (30)$$

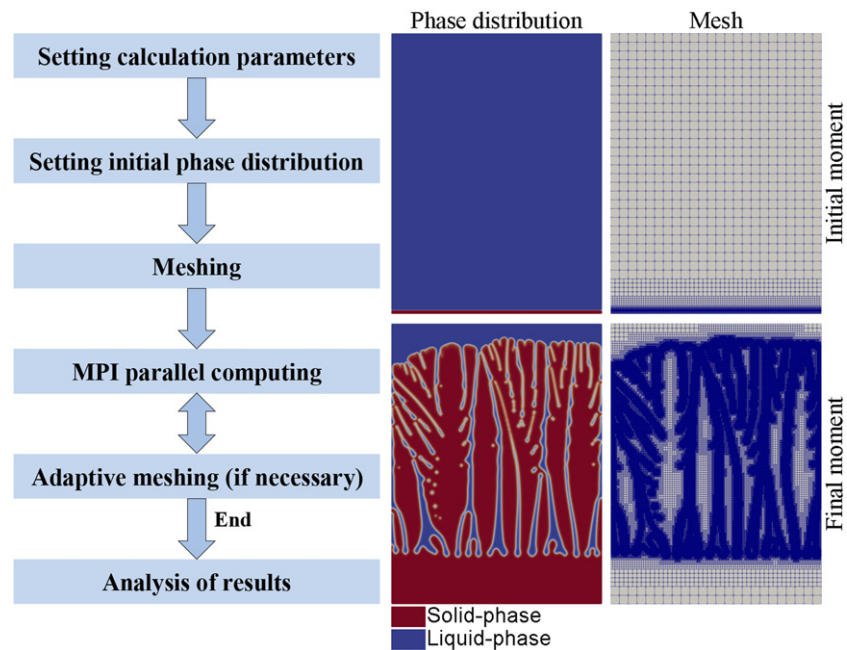


Figure 1. PFM-FEM simulation flow.

2.3. PFM-FEM simulation flow

When solving the PFM (equations (1), (12) and (13)) based on the open-source framework PRISMS-PF, only the right-end term coefficients (equations (24)–(30)) of the FE weak form of each PF variable need to be concerned, without paying much attention to the underlying logic of adaptive mesh and parallel computation, and thus the PFM can be studied more effectively for the problem of interest. Figure 1 shows the simulation flow of PFM-FEM, where the control of the adaptive mesh was based on whether the variation of the liquid–solid phase variable ϕ was drastic or not, and the parallel computational technique used message passing interface. In addition, the computing resources used are configured with the Intel Xeon Gold 6240 CPU (dual CPU, 72 threads, 128 GB RAM).

3. Results and discussion

3.1. Calculation parameters setting

The object of analysis here is the additive manufacturing process of A356 aluminum alloy. The alloy composition (mass percentage) of A356 is Al 92.7%–Si 7%–Mg 0.3%. Since the object of the PFM here is a binary alloy, the A356 aluminum alloy is treated as a pseudo-binary alloy Al 93%–Si 7%. Table 1 shows the physical properties of A356 aluminum alloy calculated using JMatPro software [35].

The effects of temperature gradient and scan rate on the microstructure evolution behavior of A356 aluminum alloy during the additive manufacturing process are focused on herein, so the adjustable calculation parameters are temperature gradient G and scan rate V_p . Table 2 shows the required calculation parameters (without G and V_p), a part of which are

Table 1. Physical properties of A356 aluminum alloy.

Parameter	Value	Unit
Density	2430	kg m ⁻³
Melting point	888.83	K
Specific heat	4900	J (kg ⁻¹ ·K ⁻¹)
Latent heat of solidification	4.3139 × 10 ⁵	J kg ⁻¹
Surface tension coefficient	0.922 55	N m ⁻¹
Solute diffusion coefficient (liquid-phase)	2.91 × 10 ⁻⁹	m ² s ⁻¹

Table 2. Required calculation parameters.

Symbol	Physical meaning	Value	Unit
ε_m	Anisotropic strength	0.03	
k	Solute redistribution coefficient	0.3	
c_0	Initial liquid-phase solute concentration	7	
U_0	Initial dimensionless supersaturation concentration	-1	
U_{off}	Initial overcooling degree of the liquid–solid interface	0.9	
y_0	Dimensionless longitudinal height of the initial liquid–solid interface	5	
a_1	Constant	0.8839	
a_2	Constant	0.6267	%
d_0	Capillary action length	8.88 × 10 ⁻⁹	m
W	Artificially specified liquid–solid interface thickness	1.77 × 10 ⁻⁷	m
D	Solute diffusion coefficient in the liquid-phase	2.91 × 10 ⁻⁹	m ² s ⁻¹
$ m_1 c_0$	Variation of liquidus temperature with solute concentration	2	K
m	Crystal system parameter	4	

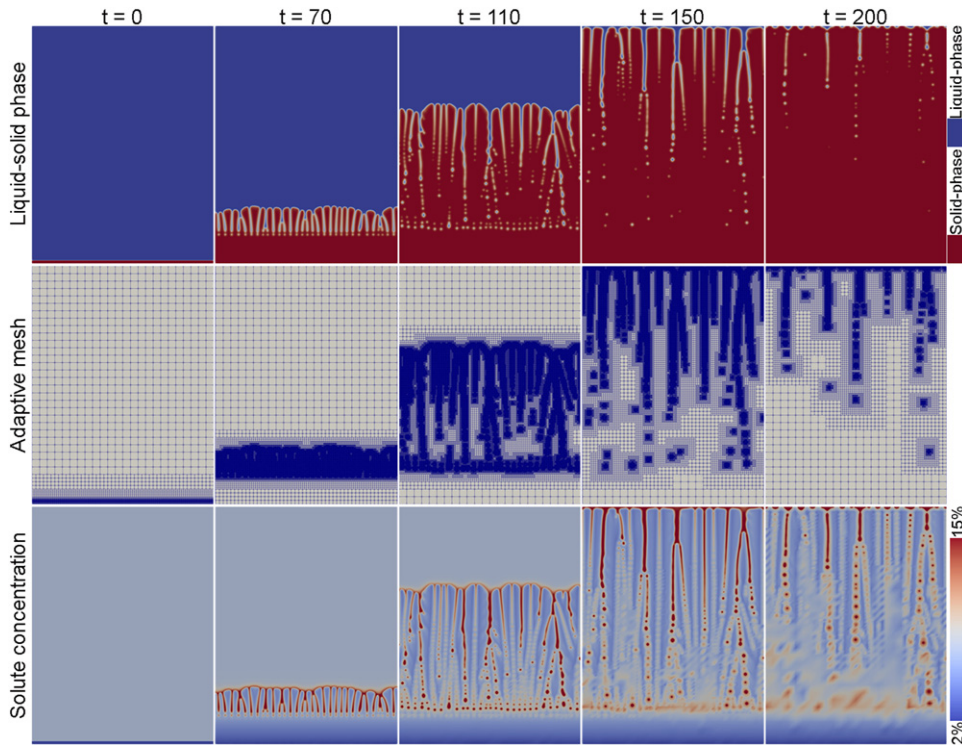
calculated by JMatPro software, a part are calculated by equation (20) and another part are obtained from reference [34], and table 3 shows the calculation schemes for different G and V_p cases. In addition, the X -directional dimension of the dimensionless computational domain is 300, the maximum refinement level of the adaptive mesh is 6 (the sizes of the maximum and minimum mesh can be 2⁶ times), and the rectangular area where the initial solid-phase is located is at the bottom and the dimensionless height is 5. It should be noted that the solute concentration, time, and length results obtained from the calculation schemes in table 3 are dimensionless, and equations (14) and (19) can be used to convert the dimensionless data to real data. The metal additive manufacturing process targeted herein is selective laser melting. Not all of the temperature gradients and scan rates given in table 3 are consistent with a real metal additive manufacturing scenario ($G \approx 10^5$ K m⁻¹, $V_p \approx 10^{-2}$ m s⁻¹), and the reason for giving a wide range of temperature gradients and scan rates is to show the special features of the metal additive manufacturing scenario in comparison.

3.2. Effects of temperature gradient and scan rate on dendrite spacing

Figure 2 shows the liquid–solid phase, adaptive mesh and solute concentration distributions at different times in *scheme C3* case. From the calculation results, it can be seen that the initial flat solid-phase interface gradually advanced at a certain temperature gradient and scan rate. Due to the existence of solute redistribution in the crystallization process, the solute concentration in front of the liquid–solid interface gradually increased; when the solute concentration at the front of the liquid–solid interface accumulated to a certain degree, the equilibrium liquidus

Table 3. Calculation schemes for different temperature gradients and scan rates cases.

V_p (m s ⁻¹) \ G (K m ⁻¹)	G (K m ⁻¹)					
	1×10^6	5×10^5	1×10^5	1×10^4	1×10^3	1×10^2
1×10^{-2}	<i>Scheme A1</i>	<i>Scheme B1</i>	<i>Scheme C1</i>	<i>Scheme D1</i>	<i>Scheme E1</i>	<i>Scheme F1</i>
8×10^{-3}	<i>Scheme A2</i>	<i>Scheme B2</i>	<i>Scheme C2</i>	<i>Scheme D2</i>	<i>Scheme E2</i>	<i>Scheme F2</i>
5×10^{-3}	<i>Scheme A3</i>	<i>Scheme B3</i>	<i>Scheme C3</i>	<i>Scheme D3</i>	<i>Scheme E3</i>	<i>Scheme F3</i>
1×10^{-3}	<i>Scheme A4</i>	<i>Scheme B4</i>	<i>Scheme C4</i>	<i>Scheme D4</i>	<i>Scheme E4</i>	<i>Scheme F4</i>
5×10^{-4}	<i>Scheme A5</i>	<i>Scheme B5</i>	<i>Scheme C5</i>	<i>Scheme D5</i>	<i>Scheme E5</i>	<i>Scheme F5</i>
1×10^{-4}	<i>Scheme A6</i>	<i>Scheme B6</i>	<i>Scheme C6</i>	<i>Scheme D6</i>	<i>Scheme E6</i>	<i>Scheme F6</i>

**Figure 2.** Liquid–solid phase, adaptive mesh and solute concentration distributions at different times in *scheme C3* case (domain size: 300×400 ; time and length: dimensionless).

temperature decreased with the increase of solute concentration, which made the composition overcooling zone appeared at a certain distance in front of the liquid–solid interface, and then led to the gradual destabilization of the flat solid-phase interface and the formation of columnar grains. When the columnar grains appeared, their projections also discharged solutes to the surrounding area, thus forming solute enrichment between the columnar grains. The typical microstructure characteristics (columnar crystals) of directional solidification

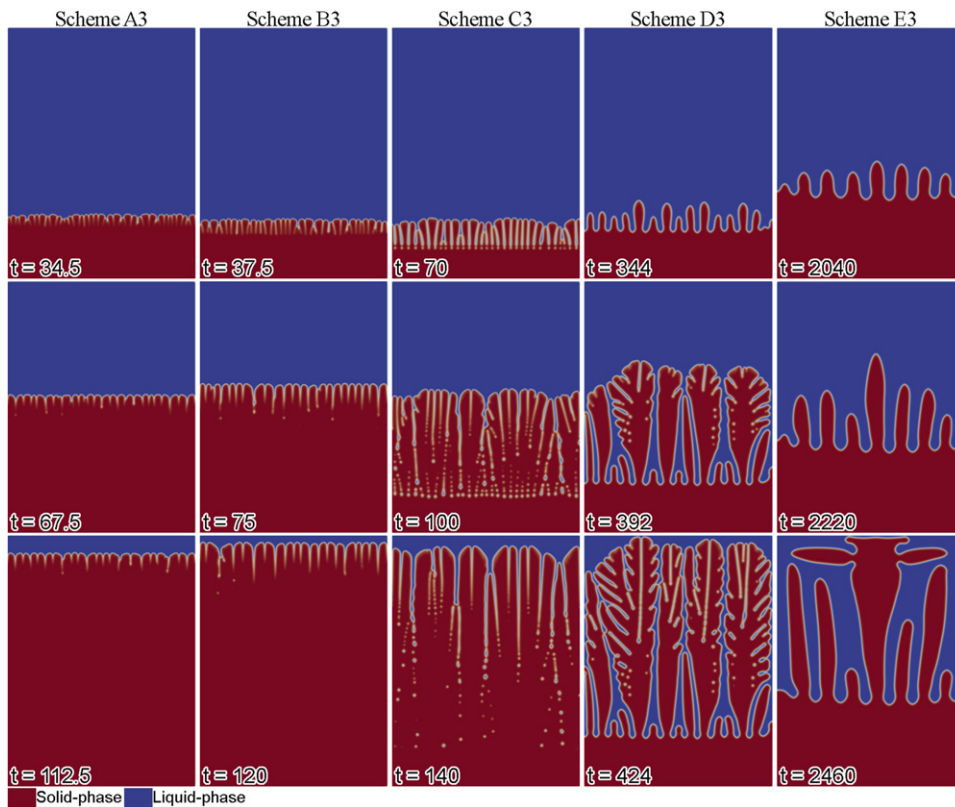


Figure 3. Liquid–solid phase distributions at different times in *schemes A3 to E3* cases (domain size: 300×400 ; time and length: dimensionless).

exhibited in figure 2 are qualitatively consistent with the experimental results of additive manufacturing of A356 alloy [36], and it can be seen that the PFM-FEM simulation process used herein can be used to study the evolutionary behavior of microstructure in additive manufacturing of A356 alloy.

Figures 3 and 4 show the results of dendrite growth at different temperature gradients and scanning rates, respectively. From the comparison results, it can be seen that the size of individual columnar grain gradually increased with the decreasing temperature gradient or scan rate; when the temperature gradient or scan rate decreased to a certain degree, eventually only individual grains were able to advance and liquid–solid interfaces with lateral growth appeared, which means that the phenomenon of grain competition growth and secondary dendrite arms appeared (*schemes D3 and E3* in figure 3; *schemes C4 and C5* in figure 4). Figure 5 shows the primary dendrite arm space data at different temperature gradients and scan rates. The results show that an increase in either the temperature gradient or the scan rate caused the primary dendrite arm space to decrease. This conclusion is consistent with the empirical equation [22] $\lambda_1 = A\Delta T_0^{0.25}G^{-0.5}V_p^{-0.25}$ for the primary dendrite arm space. Figure 6 shows the experimental results of metal additive manufacturing with different grain morphology and size under different line energy densities [37]. From the experimental comparison results, it can be seen that when the line energy density (LED, laser power divided by scan rate) was larger, the more energy was obtained by the molten pool per unit length, the larger the

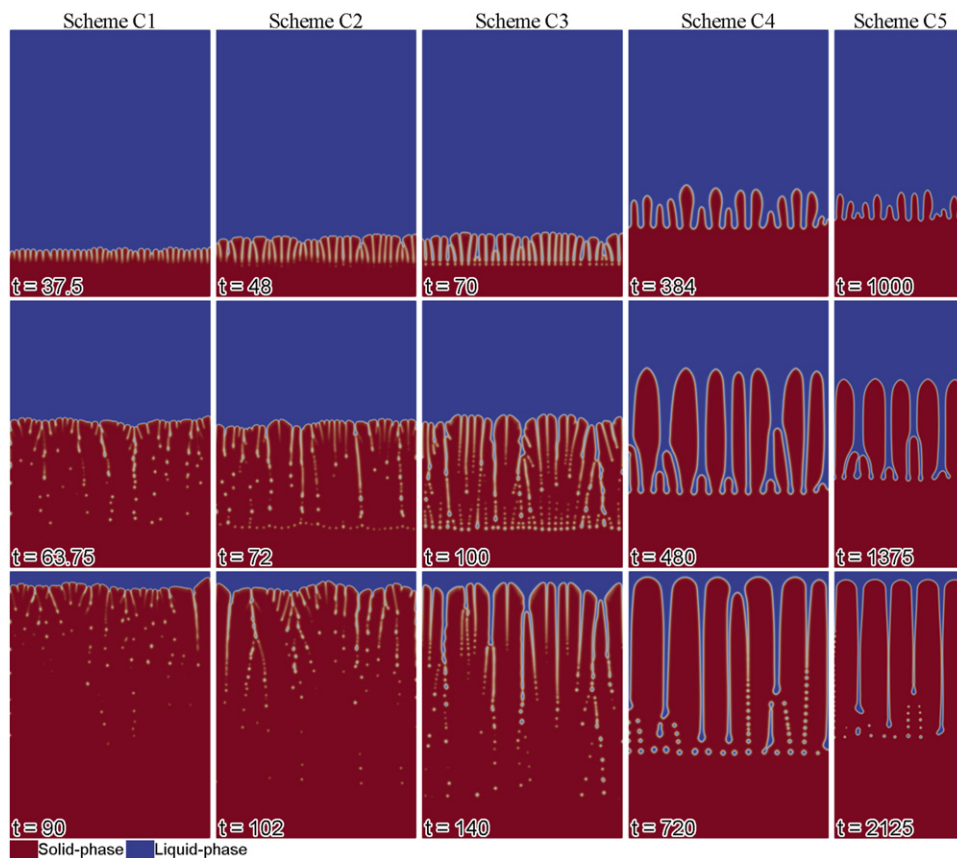


Figure 4. Liquid–solid phase distributions at different times in *schemes C1 to C5* cases (the geometry of *scheme C5* is 300×600 , and the geometry of the rest of the calculated schemes is 300×400 ; the time and length are dimensionless).

molten pool size, the smaller the overall temperature gradient exhibited, and the larger the grain size, i.e. the larger the dendrite spacing. Figure 7 shows the experimental results of the dendrite spacing (distance between the central axes of adjacent dendrite arms) change near the fusion boundary at a certain line energy density [37]. From the experimental results, it can be seen that the dendrite spacing became smaller and then larger as the grains passed through the fusion boundary along the building direction. The reason for this is that the temperature gradient at the molten pool boundary varies during solidification. Generally speaking, when the molten pool has the largest boundary (the location of the fusion boundary), the temperature gradient is the largest; as the molten pool boundary shrinks, the temperature gradient gradually decreases, so the experimental results show that the dendrite spacing above the fusion boundary was the smallest. The above experimental results verified the effect of process parameters on the dendrite spacing.

3.3. Effects of temperature gradient and scan rate on dendrite morphology

Considering that the microstructure evolution behavior of the molten pool in the process of metal additive manufacturing has certain similarities with the laser welding process, and the

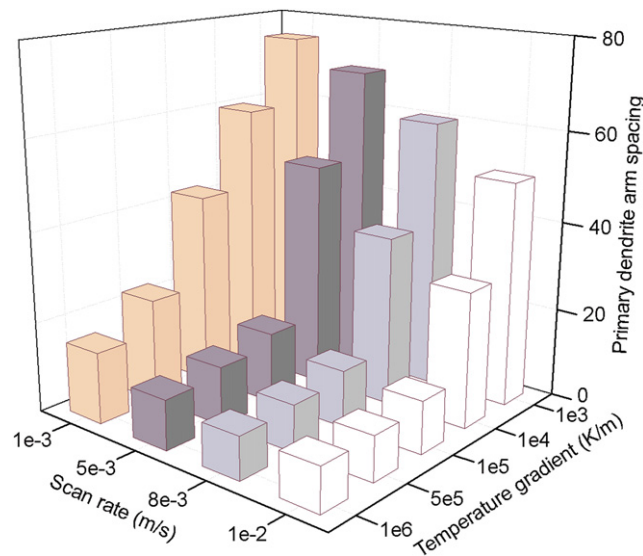


Figure 5. Primary dendrite arm space at different temperature gradients and scan rates (the primary dendrite arm spacing is dimensionless).

laser welding field usually uses the ratio of temperature gradient to scan rate (that is G/V_p) to study the impact of the forming process on the dendrite morphology [38], so the influence of temperature gradient and scan rate on the evolution of the dendrite morphology in the solidification process of metal additive manufacturing is analyzed here based on the ratio G/V_p . Figures 8 and 9 show the dendrite morphology and solute concentration distributions at different temperature gradients and scan rates, respectively. The reason for the larger Y -directional size when the scan rate was lower is that the solute concentration at the front of the solidification interface grew at a slower rate, making it necessary to advance the solidification interface upward for a longer distance before a morphological change was possible. From the calculation results, it can be seen that when the temperature gradient G was maintained at a certain level, the overall trend of the solidification morphology changed gradually from flat crystal to cellular crystal, columnar crystal, or even dendritic structure as the scan rate V_p gradually increased, i.e. the ratio G/V_p gradually decreased; when V_p was maintained at a certain level, the overall trend of the solidification morphology also showed a gradual change from flat crystal to cellular crystal, columnar crystal, or even dendritic structure, as G gradually decreased, i.e. the ratio G/V_p gradually decreased. The conclusion and the evolution of laser welding microstructure are in general agreement on the trend, that is, as the ratio G/V_p gradually decreases, the solidification morphology gradually changes from flat crystal to cellular crystal, columnar crystal, dendritic crystal, and even equiaxial crystal [38]. It should be noted that in figure 8, when the temperature gradient was smallest ($G = 1 \times 10^2 \text{ K m}^{-1}$), the overall dendrite morphology showed flat crystal, which seems to be inconsistent with the above conclusion and will be explained later herein.

The reason why temperature gradient and scan rate affect the dendrite morphology in the ratio G/V_p is essentially because the temperature gradient and scan rate together determine the size of the composition overcooling zone in front of the liquid–solid interface. Because of the solute redistribution phenomenon during solidification, the solute concentration in the liquid-phase increases within a certain distance in front of the liquid–solid interface, and because

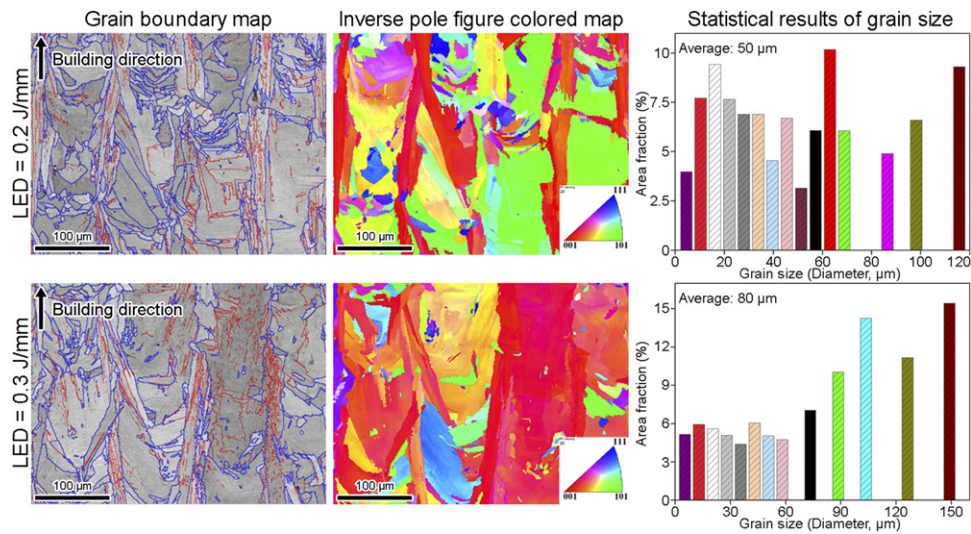


Figure 6. Experimental results of grain morphology and size under different line energy densities [37] (selective laser melting of IN738 superalloy; the microstructures were taken on the locations away from the fusion boundary; the grain sizes were measured by the dedicated software OIM; the blue color in the grain boundary map denotes grain boundaries with orientation difference greater than 10 degree, and the red color denotes grain boundaries with orientation difference between 2 degree and 10 degree).

the equilibrium liquidus temperature of the alloy decreases with the increase of the solute concentration, which leads to a lower equilibrium liquidus temperature in front of the liquid–solid interface compared with other regions of the liquid-phase. The so-called composition overcooling zone refers to the fact that the equilibrium liquidus temperature of the liquid-phase at a certain distance in front of the liquid–solid interface is lower than the actual temperature of the liquid-phase. When the composition overcooling zone is small, or even non-existent, the forward-growing grains are re-melted by the ‘superheated’ liquid metal, dendritic fronts can only form cellular crystal, or even flat crystal; when the composition overcooling zone is large, the forward-growing grains can be retained, and then developed into columnar crystal, dendrite crystal, or even nucleation inside the liquid-phase directly to form equiaxed crystal.

Figure 10 shows the schematic diagram of the effects of temperature gradient and scan rate on the composition overcooling zone. The three dashed lines in figure 10 represent the actual temperature distributions of the liquid-phase in front of the liquid–solid interface at different temperature gradients, and it is easy to know that the actual temperature of the liquid-phase in front of the liquid–solid interface increases with the increase of the temperature gradient. The three solid curves in figure 10 represent the equilibrium liquidus temperature distributions in front of the liquid–solid interface at different scan rates. With the increase of scan rate, the dendrite growth rate accelerates and the solute redistribution phenomenon deviates more and more from the equilibrium solidification process, which shows that the solid-phase solute concentration increases while the liquid-phase solute concentration decreases, making the equilibrium liquidus temperature in front of the liquid–solid interface increase as a whole. When the scan rate is certain (taking $V_p = V_{p_{mid}}$ as an example), with the increase

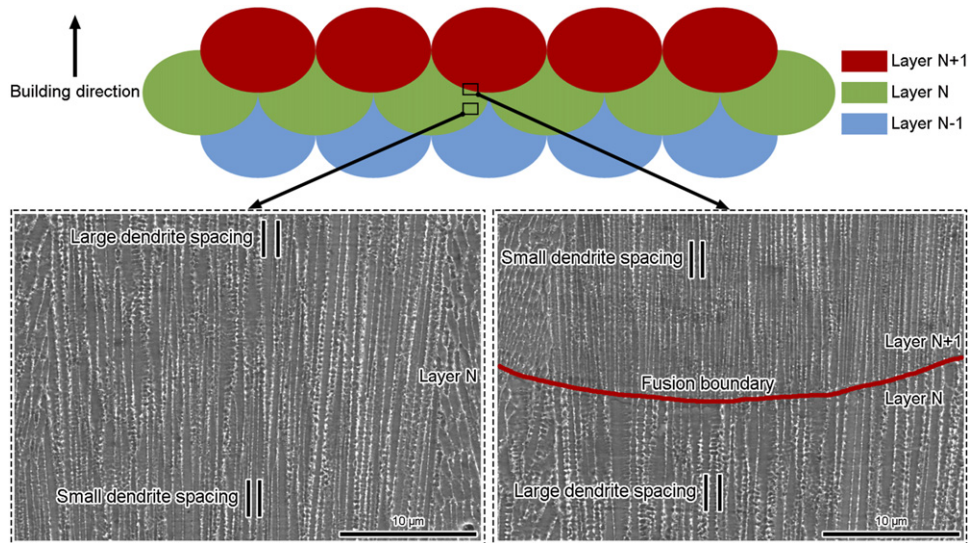


Figure 7. Experimental results on the variation of dendrite spacing near the fusion boundary under a LED of 0.2 J mm^{-1} [37] (selective laser melting of IN738 superalloy with the LED of 0.2 J mm^{-1}).

of temperature gradient, the composition overcooling zone gradually decreases or even disappears, which makes the solidification morphology transform from dendrite crystal to columnar crystal, cellular crystal, or even flat crystal. When the temperature gradient is certain (taking $G = G_{\text{mid}}$ as an example), with the increase of scan rate, the composition overcooling zone gradually increases, which makes the solidification morphology transform from flat crystal to cellular crystal, columnar crystal, dendrite crystal, and even equiaxial crystal. In figure 8, when the temperature gradient was smallest ($G = 1 \times 10^2 \text{ K m}^{-1}$), the dendrite morphology as a whole behaved as flat crystal. The reason is that the PFM here did not consider nucleation, which could not be directly nucleated from the liquid-phase and developed into equiaxed crystal. In fact, the temperature gradient during the metal additive manufacturing solidification process is roughly between 10^4 K m^{-1} and 10^6 K m^{-1} , so the equiaxed crystal accounts for a very small percentage of the microstructure. Figure 11 shows the experimental results of grain morphology under different line energy densities [37]. From the experimental results, it can be seen that when the line energy density was larger, the overall temperature gradient of the molten pool was smaller and the composition overcooling zone is larger, so the secondary dendrite arm appeared; while when the line energy density was smaller, the secondary dendrite arm did not appear. The above experimental results verified the effect of process parameters on the grain morphology.

3.4. Effect of initial solid-phase morphology on dendrite growth

In order to analyze the influence of the initial solid-phase morphology on the dendrite growth, the calculation of the non-flat initial solid-phase morphology cases was carried out as shown in table 4, where the initial solid-phase interface was a flat interface plus three small semicircular bumps. Figure 12 shows the liquid–solid phase, adaptive mesh and solute concentration distributions at different times in *scheme H2* case. From the calculation results, it can be

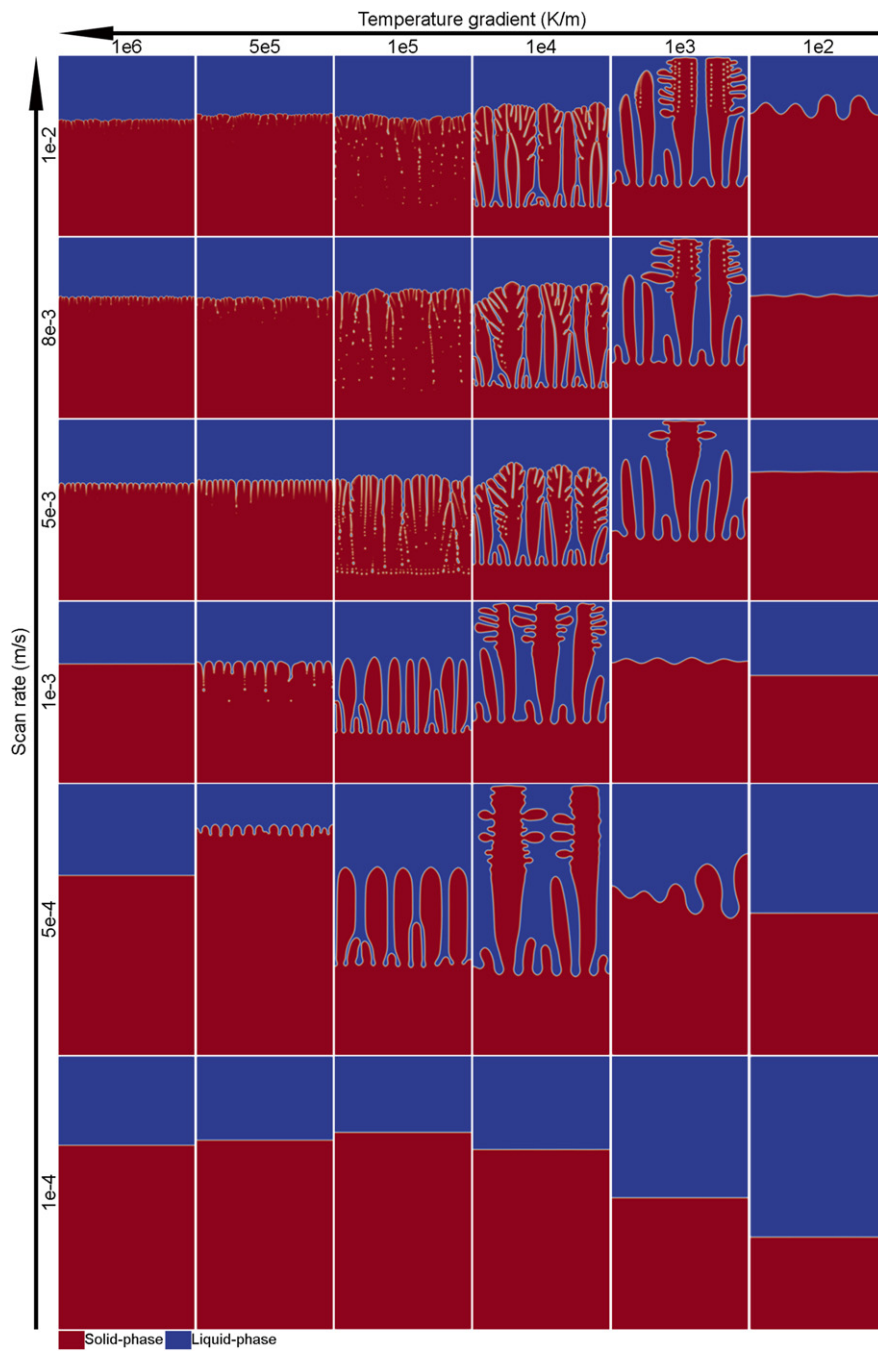


Figure 8. Dendrite morphology at different temperature gradients and scan rates (when the scan rate are 5×10^{-4} and 1×10^{-4} m s⁻¹, the domain size is 300×600 , and the rest is 300×400 ; the time and length are dimensionless).

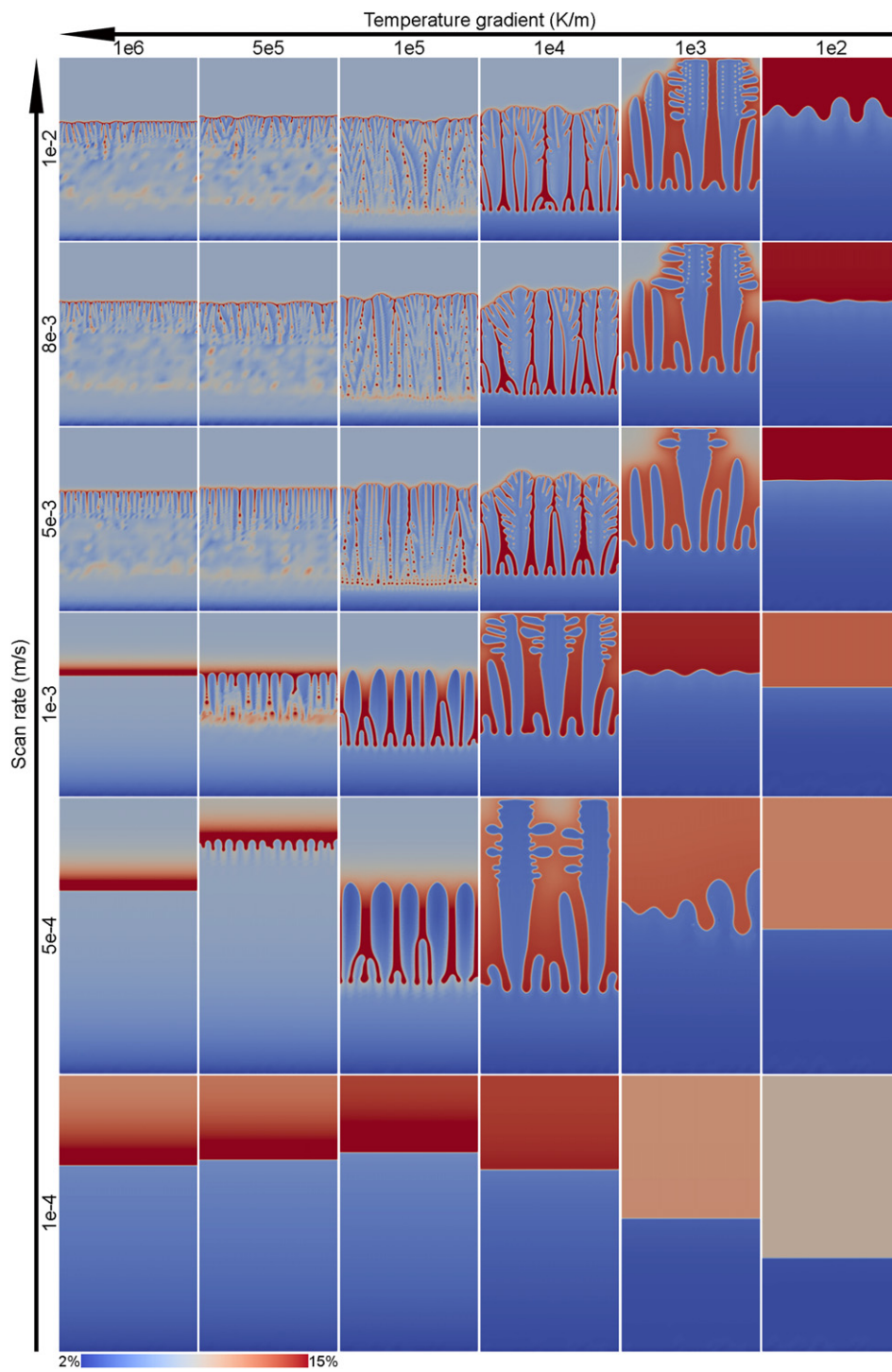


Figure 9. Solute concentration distributions at different temperature gradients and scan rates (when the scan rate are 5×10^{-4} and 1×10^{-4} m s⁻¹, the domain size is 300×600 , and the rest is 300×400 ; the time and length are dimensionless).

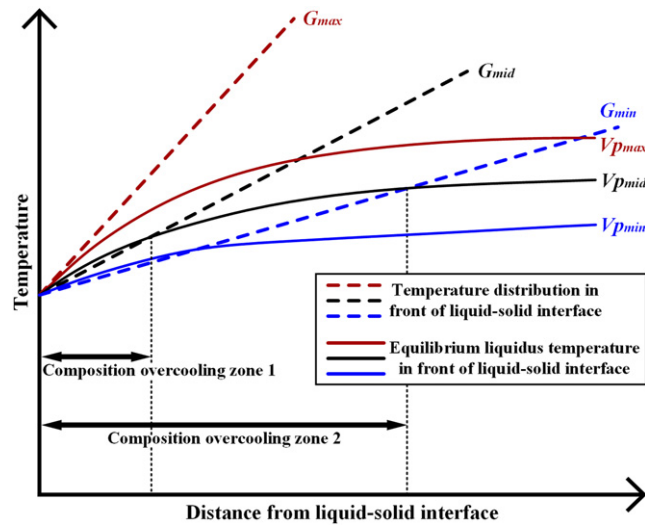


Figure 10. Schematic diagram of the effects of temperature gradient and scan rate on the composition overcooling zone (G_{\max} , G_{mid} , G_{\min} represent high, medium, and low temperature gradients, respectively, and $V_{p_{\max}}$, $V_{p_{\text{mid}}}$, $V_{p_{\min}}$ represent high, medium, and low scan rates, respectively).

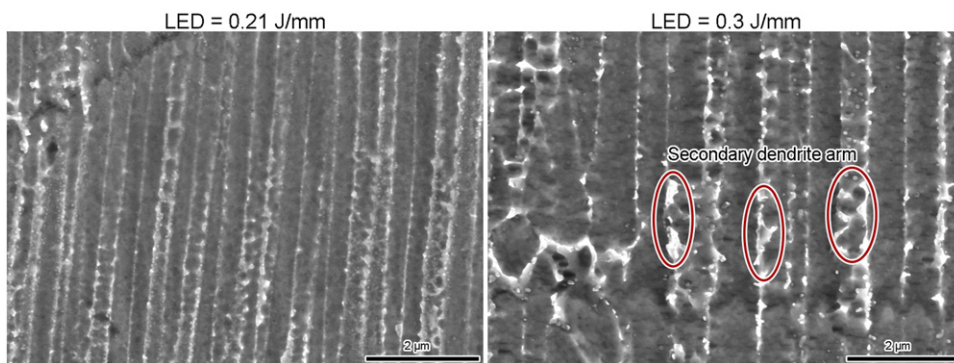


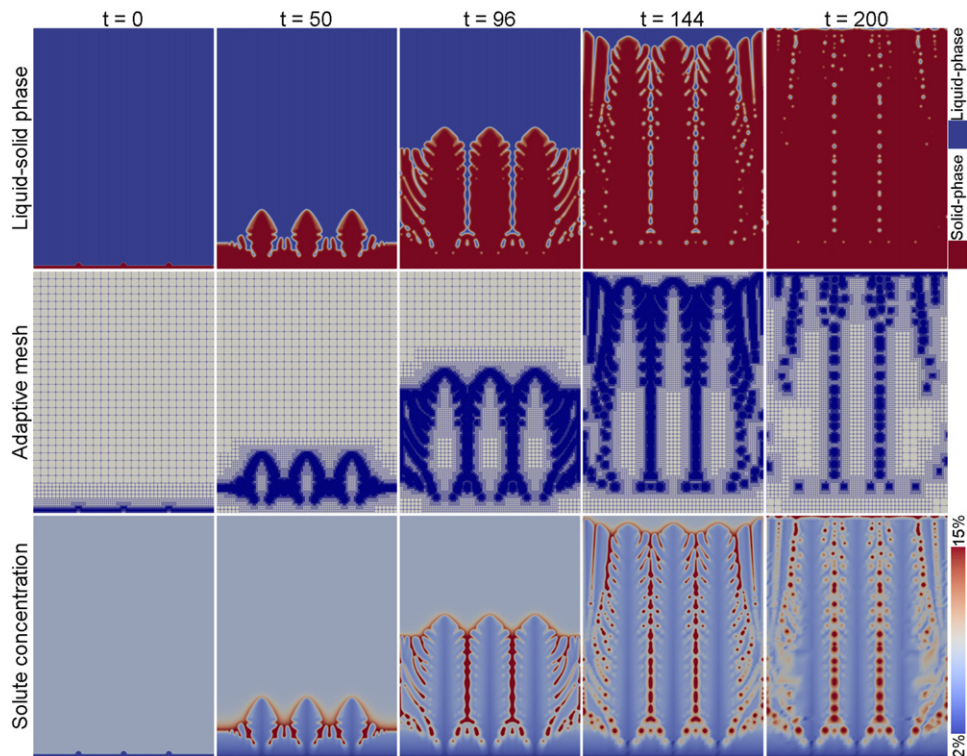
Figure 11. Experimental results of grain morphology under different line energy densities [37] (selective laser melting of IN738 superalloy).

seen that compared to *scheme C3* case (figure 2), the dendrites were obviously affected during the subsequent growth process due to the presence of three small bumps at the initial solid-phase interface.

Figures 13 and 14 show the dendrite morphology and solute concentration distributions at different temperature gradients and scan rates, respectively. From the calculation results, it can be seen that as the ratio G/V_p gradually decreased, the greater the influence of the initial solid-phase morphology on the dendrite growth. The reason for this still needs to start from the rule of the effect of temperature gradient and scan rate on the composition overcooling zone as revealed in figure 10. When the ratio G/V_p is large, the composition overcooling zone in front of the liquid–solid interface is small, and it is difficult for the dendrites to penetrate into

Table 4. Calculation schemes for the cases of non-flat initial solid-phase morphology.

V_p (m s ⁻¹) \ G (K m ⁻¹)	G (K m ⁻¹)		
	1×10^6	1×10^5	1×10^2
1×10^{-2}	<i>Scheme G1</i>	<i>Scheme H1</i>	<i>Scheme J1</i>
5×10^{-3}	<i>Scheme G2</i>	<i>Scheme H2</i>	<i>Scheme J2</i>
1×10^{-4}	<i>Scheme G3</i>	<i>Scheme H3</i>	<i>Scheme J3</i>

**Figure 12.** Liquid–solid phase, adaptive mesh and solute concentration distributions at different times in *scheme H2* case (domain size: 300×400 ; time and length: dimensionless).

the liquid-phase based on the non-flat initial solid-phase interface, and then the development is no different from the flat initial solid-phase interface situation; when the ratio G/V_p is small, the composition overcooling zone in front of the liquid–solid interface is large, and it is easy for the dendrites to penetrate into the liquid-phase based on the non-flat initial solid-phase interface, and then the development is more different from the flat initial solid-phase interface situation.

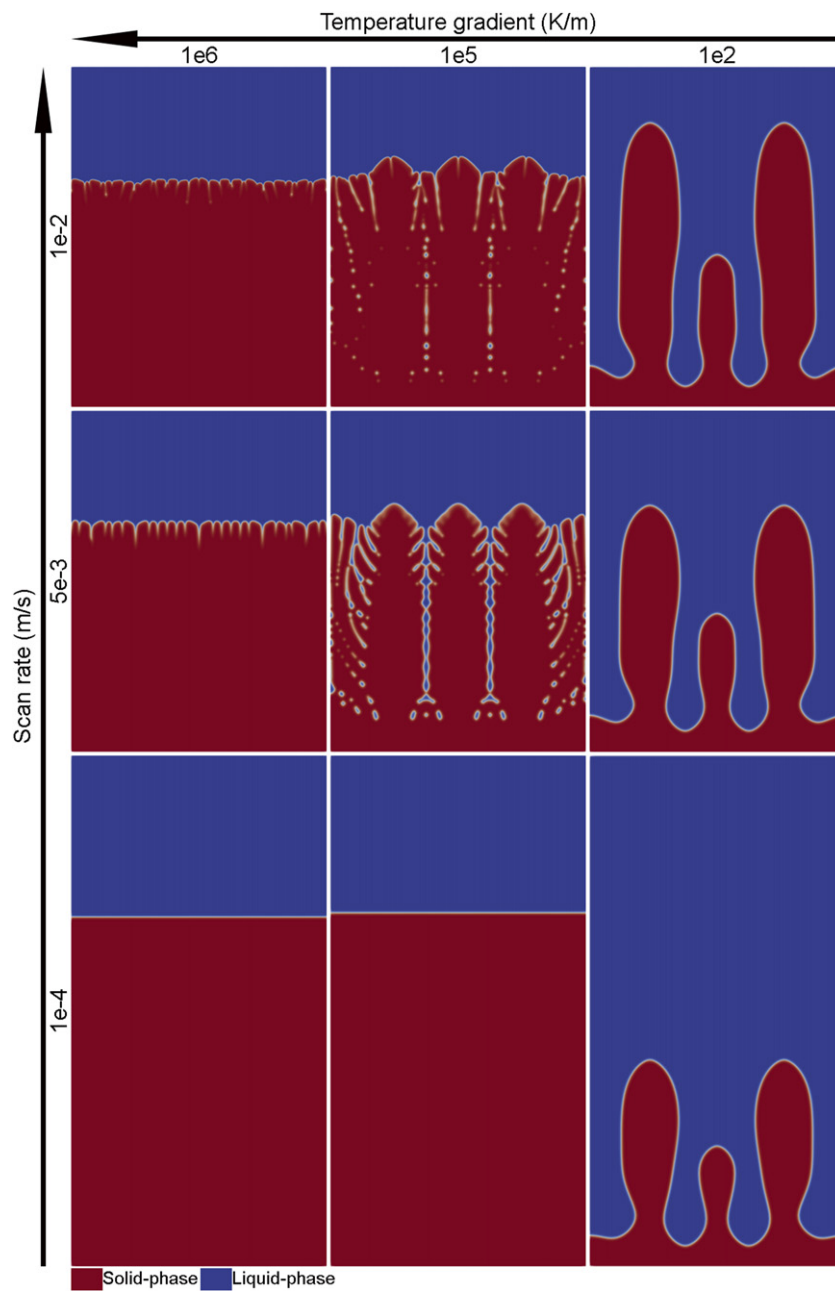


Figure 13. Dendrite morphology at different temperature gradients and scan rates (when the scan rate is $1 \times 10^{-4} \text{ m s}^{-1}$, the domain size is 300×600 , and the rest is 300×400 ; the time and length are dimensionless).

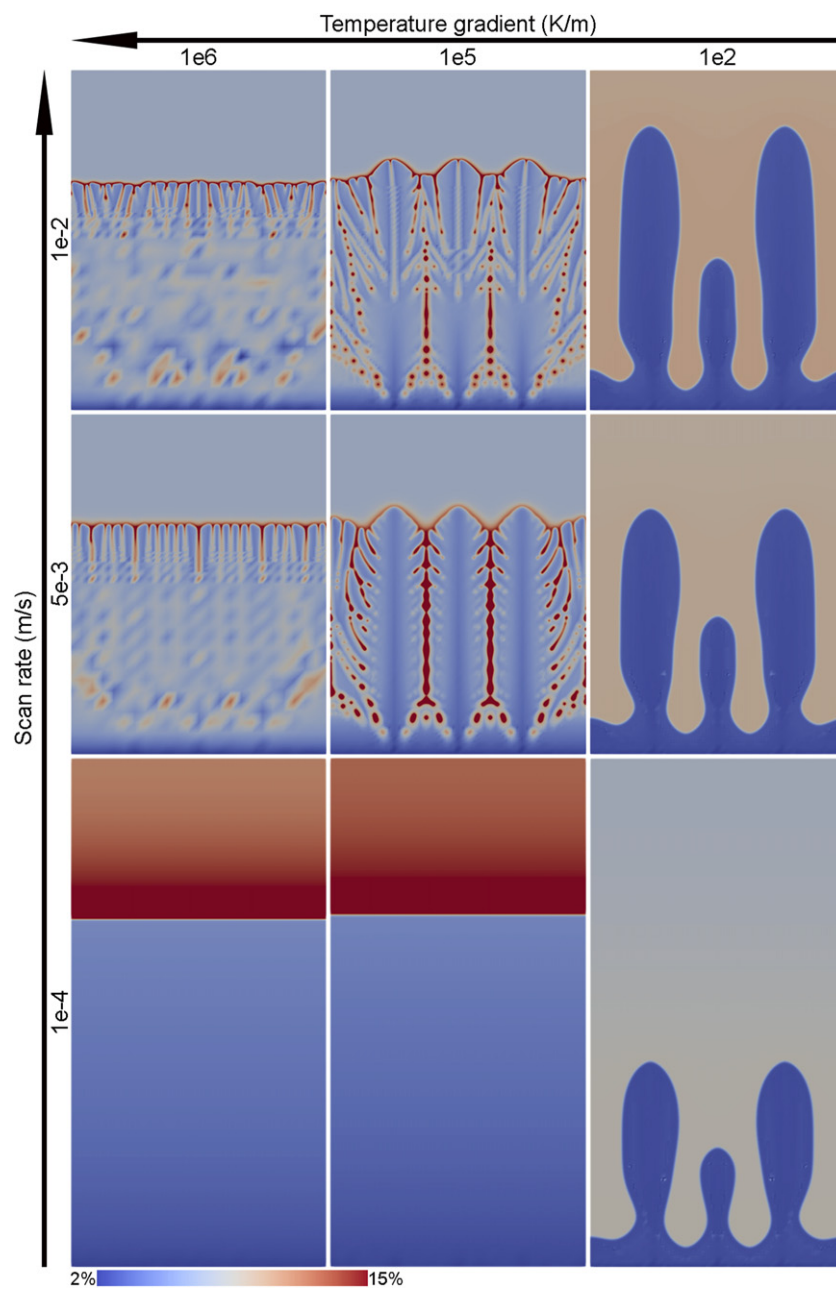


Figure 14. Solute concentration distributions at different temperature gradients and scan rates (when the scan rate is $1 \times 10^{-4} \text{ m s}^{-1}$, the domain size is 300×600 , and the rest is 300×400 ; the time and length are dimensionless).

4. Conclusions

- (a) Based on the open-source PFM framework PRISMS-PF, the PFM-FEM simulation flow for the solidification process of A356 aluminum alloy additive manufacturing in the two-dimensional case was established herein, and the effects of temperature gradient, scan rate and initial solid-phase morphology on solute concentration, dendrite spacing and dendrite morphology were analyzed.
- (b) Comparing the calculation results for different temperature gradient and scan rate cases, it was found that the increase of temperature gradient G or scan rate V_p decreased the primary dendrite arm space. As the ratio G/V_p gradually decreased, the solidification morphology gradually changed from flat crystal to cellular crystal, columnar crystal, and even dendrite crystal, and the reason is that as the scan rate increases or the temperature gradient decreases, the composition overcooling zone will increase.
- (c) Comparing the calculation results for different initial solid-phase morphology cases, it was found that the influence of initial solid-phase morphology on dendrite growth increased as the ratio G/V_p decreased, and the influence rule is also related to the composition overcooling zone under different conditions. When the composition overcooling zone in front of the liquid–solid interface is large, it is easy for the dendrites to penetrate into the liquid-phase based on the non-flat initial solid-phase interface.

Acknowledgment

This work was supported by the Basic and Applied Basic Research Project of Guangzhou Basic Research Program (No. 202102020724) and the Natural Science Foundation of Guangdong Province (No. 2019A1515012040).

Conflict of interest

The authors declare that they have no conflicts of interest to report regarding the present study.

Data availability statement

All data that support the findings of this study are included within the article (and any supplementary files).

ORCID iDs

Liu Cao  <https://orcid.org/0000-0002-3662-6633>

Rui-Fan Meng  <https://orcid.org/0000-0002-7799-1549>

References

- [1] Cooke S, Ahmadi K, Willerth S and Herring R 2020 Metal additive manufacturing: technology, metallurgy and modelling *J. Manuf. Process.* **57** 978–1003
- [2] Sing S L and Yeong W Y 2020 Laser powder bed fusion for metal additive manufacturing: perspectives on recent developments *Virtual Phys. Prototyp.* **15** 359–70

- [3] Hashemi S M, Parvizi S, Baghbanijavid H, Tan A T L, Nematollahi M, Ramazani A, Fang N X and Elahinia M 2022 Computational modelling of process-structure-property-performance relationships in metal additive manufacturing: a review *Int. Mater. Rev.* **67** 1–46
- [4] Smith J, Xiong W, Yan W, Lin S, Cheng P, Kafka O L, Wagner G J, Cao J and Liu W K 2016 Linking process, structure, property, and performance for metal-based additive manufacturing: computational approaches with experimental support *Comput. Mech.* **57** 583–610
- [5] Guo Q *et al* 2020 *In situ* full-field mapping of melt flow dynamics in laser metal additive manufacturing *Addit. Manuf.* **31** 100939
- [6] Everton S K, Hirsch M, Stravroulakis P, Leach R K and Clare A T 2016 Review of *in situ* process monitoring and *in situ* metrology for metal additive manufacturing *Mater. Des.* **95** 431–45
- [7] Li J, Zhou X, Brochu M, Provas N and Zhao Y F 2020 Solidification microstructure simulation of Ti-6Al-4V in metal additive manufacturing: a review *Addit. Manuf.* **31** 100989
- [8] Kundin J, Ramazani A, Prah U and Haase C 2019 Microstructure evolution of binary and multicomponent manganese steels during selective laser melting: phase-field modeling and experimental validation *Metall. Mat. Trans. A* **50** 2022–40
- [9] Sahoo S and Chou K 2016 Phase-field simulation of microstructure evolution of Ti-6Al-4V in electron beam additive manufacturing process *Addit. Manuf.* **9** 14–24
- [10] Kubo J, Koizumi Y, Ishimoto T and Nakano T 2021 Modified cellular automaton simulation of metal additive manufacturing *Mater. Trans.* **62** 864–70
- [11] Zhang J, Liou F, Seufzer W and Taminger K 2016 A coupled finite element cellular automaton model to predict thermal history and grain morphology of Ti-6Al-4V during direct metal deposition (DMD) *Addit. Manuf.* **11** 32–9
- [12] Pal P, Abhishek G S and Karagadde S 2020 A Monte Carlo approach to simulate dendritic microstructures during binary alloy solidification *Modelling Simul. Mater. Sci. Eng.* **28** 085001
- [13] Wang R, Liu Y and Wei D Q 2014 Microstructures in solidification simulation of electron beam scanning with MC in molten pool *Adv. Mater. Res.* **898** 168–72
- [14] Keller T *et al* 2017 Application of finite element, phase-field, and CALPHAD-based methods to additive manufacturing of Ni-based superalloys *Acta Mater.* **139** 244–53
- [15] Gong X and Chou K 2015 Phase-field modeling of microstructure evolution in electron beam additive manufacturing *JOM* **67** 1176–82
- [16] Akram J, Chalavadi P, Pal D and Stucker B 2018 Understanding grain evolution in additive manufacturing through modeling *Addit. Manuf.* **21** 255–68
- [17] Lian Y, Gan Z, Yu C, Kats D, Liu W K and Wagner G J 2019 A cellular automaton finite volume method for microstructure evolution during additive manufacturing *Mater. Des.* **169** 107672
- [18] Rolchigo M R and LeSar R 2018 Modeling of binary alloy solidification under conditions representative of additive manufacturing *Comput. Mater. Sci.* **150** 535–45
- [19] Zhu Y and Pan X 2014 Kinetic Monte Carlo simulation of 3D growth of NiTi alloy thin films *Appl. Surf. Sci.* **321** 24–9
- [20] Geng R-W, Du J, Wei Z-Y and Zhao G-X 2017 Simulation of microstructure evolution in fused-coating additive manufacturing based on phase field approach *China Foundry* **14** 346–52
- [21] Zhang J, Wu L M, Zhang Y and Meng L B 2019 Phase field simulation of dendritic microstructure in additively manufactured titanium alloy *Metal Powder Rep.* **74** 20–4
- [22] Fallah V, Amoozrezaei M, Provas N, Corbin S F and Khajepour A 2012 Phase-field simulation of solidification morphology in laser powder deposition of Ti-Nb alloys *Acta Mater.* **60** 1633–46
- [23] Greenwood M, Shampur K N, Ofori-Opoku N, Pinomaa T, Wang L, Gurevich S and Provas N 2018 Quantitative 3D phase field modelling of solidification using next-generation adaptive mesh refinement *Comput. Mater. Sci.* **142** 153–71
- [24] Sakane S, Takaki T, Rojas R, Ohno M, Shibuta Y, Shimokawabe T and Aoki T 2017 Multi-GPUs parallel computation of dendrite growth in forced convection using the phase-field-lattice Boltzmann model *J. Cryst. Growth* **474** 154–9
- [25] Guo Z and Xiong S M 2015 On solving the 3D phase field equations by employing a parallel-adaptive mesh refinement (Para-AMR) algorithm *Comput. Phys. Commun.* **190** 89–97
- [26] Ding P and Liu Z 2020 Accelerating phase-field modeling of solidification with a parallel adaptive computational domain approach *Int. Commun. Heat Mass Transfer* **111** 104452
- [27] Tonks M R, Gaston D, Millett P C, Andrs D and Talbot P 2012 An object-oriented finite element framework for multiphysics phase field simulations *Comput. Mater. Sci.* **51** 20–9
- [28] Tegeler M, Shchyglo O, Kamachali R D, Monas A, Steinbach I and Sutmann G 2017 Parallel multiphase field simulations with OpenPhase *Comput. Phys. Commun.* **215** 173–87

- [29] Guyer J E, Wheeler D and Warren J A 2009 FiPy: partial differential equations with Python *Comput. Sci. Eng.* **11** 6–15
- [30] Kleiven D and Akola J 2020 Precipitate formation in aluminium alloys: multi-scale modelling approach *Acta Mater.* **195** 123–31
- [31] DeWitt S, Rudraraju S, Montiel D, Andrews W B and Thornton K 2020 PRISMS-PF: a general framework for phase-field modeling with a matrix-free finite element method *npj Comput. Mater.* **6** 29
- [32] Aagesen L K *et al* 2018 PRISMS: an integrated, open-source framework for accelerating predictive structural materials science *JOM* **70** 2298–314
- [33] Arndt D *et al* 2021 The deal.II finite element library: design, features, and insights *Comput. Math. Appl.* **81** 407–22
- [34] Echebarria B, Folch R, Karma A and Plapp M 2004 Quantitative phase-field model of alloy solidification *Phys. Rev. E* **70** 061604
- [35] Saunders N, Guo U K Z, Li X, Miodownik A P and Schillé J-P 2003 Using JMatPro to model materials properties and behavior *JOM* **55** 60–5
- [36] Kimura T and Nakamoto T 2016 Microstructures and mechanical properties of A356 (AlSi₇Mg_{0.3}) aluminum alloy fabricated by selective laser melting *Mater. Des.* **89** 1294–301
- [37] Zhang L, Li Y, Zhang S and Zhang Q 2021 Selective laser melting of IN738 superalloy with a low Mn + Si content: effect of energy input on characteristics of molten pool, metallurgical defects, microstructures and mechanical properties *Mater. Sci. Eng. A* **826** 141985
- [38] Wang L 2018 Phase field investigation on microstructure evolution in the laser welding pool of 2A14 aluminum alloy *Doctor Thesis* Nanjing University of Aeronautics and Astronautics